PROCEEDINGS A

royalsocietypublishing.org/journal/rspa

Research

Cite this article: Van Loock F, Bernardo V, Rodríguez Pérez MA, Fleck NA. 2019 The mechanics of solid-state nanofoaming. *Proc. R. Soc. A* **475**: 20190339.
http://dx.doi.org/10.1098/rspa.2019.0339

Received: 30 May 2019
Accepted: 27 August 2019

Subject Areas:
materials science, mechanical engineering

Keywords:
solid-state foaming, PMMA nanofoams, molecular weight, void growth model, porosity limit, deformation mechanism maps

Author for correspondence:
Norman A. Fleck
e-mail: naf1@eng.cam.ac.uk

Electronic supplementary material is available online at https://dx.doi.org/10.6084/m9.figshare.c.4663595.

THE ROYAL SOCIETY PUBLISHING

The mechanics of solid-state nanofoaming

Frederik Van Loock[1], Victoria Bernardo[2], Miguel Angel Rodríguez Pérez[2] and Norman A. Fleck[1]

[1]Department of Engineering, University of Cambridge, Trumpington Street, CB2 1PZ Cambridge, UK
[2]Cellular Materials Laboratory (CellMat), Condensed Matter Physics Department, University of Valladolid, Paseo de Belen 7, 47011 Valladolid, Spain

NAF, 0000-0003-0224-1804

Solid-state nanofoaming experiments are conducted on two polymethyl methacrylate (PMMA) grades of markedly different molecular weight using CO_2 as the blowing agent. The sensitivity of porosity to foaming time and foaming temperature is measured. Also, the microstructure of the PMMA nanofoams is characterized in terms of cell size and cell nucleation density. A one-dimensional numerical model is developed to predict the growth of spherical, gas-filled voids during the solid-state foaming process. Diffusion of CO_2 within the PMMA matrix is sufficiently rapid for the concentration of CO_2 to remain almost uniform spatially. The foaming model makes use of experimentally calibrated constitutive laws for the uniaxial stress versus strain response of the PMMA grades as a function of strain rate and temperature, and the effect of dissolved CO_2 is accounted for by a shift in the glass transition temperature of the PMMA. The maximum achievable porosity is interpreted in terms of cell wall tearing and comparisons are made between the predictions of the model and nanofoaming measurements; it is deduced that the failure strain of the cell walls is sensitive to cell wall thickness.

1. Introduction

Polymeric nanofoams are polymer foams with an average cell size below 1 µm [1]. This new class of porous solids has the potential to offer unique and attractive combinations of thermal, mechanical and optical properties [2–4]. For example, the thermal conductivity λ of polymeric nanofoams may be lower

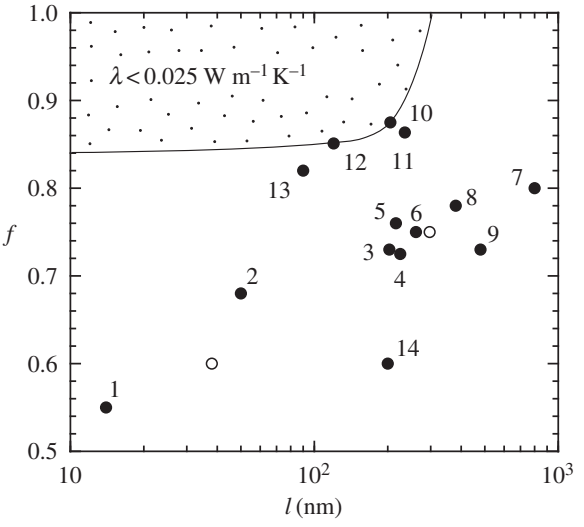

Figure 1. Reported porosity f versus void size l of high porosity (PMMA-based) nanofoams produced via solid-state foaming. The 'open circles' refer to results obtained in the present study. The 'filled circles' refer to data retrieved from [4,9–17]; see the electronic supplementary material information for the reference corresponding to a data point.

than the value for air, $\lambda = 0.025\,\mathrm{W\,m^{-1}\,K^{-1}}$: when the average cell size is of the order of the mean free path of the gas molecules in the cells (close to 70 nm for air at standard conditions), the thermal conductivity of the gas in the foam is significantly reduced due to the Knudsen effect [5,6]. A polymeric nanofoam may have a thermal conductivity close to or below $0.025\,\mathrm{W\,m^{-1}\,K^{-1}}$ when the average cell size l is below 200 nm and the porosity f exceeds 0.85; see, for example, Wang *et al.* [7]. To achieve this morphology, the cell nucleation density N_d must exceed $10^{21}\,\mathrm{m^{-3}}$ [1].

A large number of experimental studies focus on the effect of processing conditions and the choice of polymer precursor upon the cell nucleation density N_d, the void size l and the porosity f of polymeric nanofoams, as reviewed by Costeux [1]. Many of these studies employ the solid-state foaming method in which a physical blowing agent (e.g. CO_2) is used to nucleate and grow cells in a polymer matrix such as polymethyl methacrylate (PMMA) [8,9]. The available data on the cell size and porosity that have been achieved to date for high porosity (PMMA-based) polymeric nanofoams via solid-state foaming are summarized in figure 1. Data are retrieved from [4,9–17]. It is clear that the ideal combination of high porosity ($f > 0.85$) and small cell size ($l < 200$ nm) is yet to be achieved. Polymeric nanofoams of porosity of the order of 0.8–0.9 have been produced, but their cell size is above 200 nm (and $N_\mathrm{d} < 10^{21}\,\mathrm{m^{-3}}$). By contrast, polymeric nanofoams of $l < 200$ nm are reported for a nucleation density above $10^{21}\,\mathrm{m^{-3}}$, but their porosity is limited to close to 0.85. Recently, manufacturing techniques have evolved to combine solid-state nanofoaming and injection moulding in an attempt to improve the mechanical properties and surface properties of injection moulded foams, but these nanofoams have porosities well below 0.5 [18].

The observed porosity limit for nanofoams with a nucleation density above $10^{21}\,\mathrm{m^{-3}}$ may be due to the fact that the minimum wall thickness between nano-sized cells is dictated by the end-to-end distance of the individual polymer chains [1,12]. An aim of the present study is to gain scientific insight into this limiting behaviour, and thereby suggest ways of overcoming this barrier, if possible.

The final porosity and final cell size in *solid-state* nanofoaming requires a solid mechanics analysis of void growth. A substantial body of experimental work has now been performed on polymeric nanofoams produced via solid-state foaming (recall figure 1 and the review by Costeux [1]), and several analyses have been developed for cell growth in liquid-state foaming

processes [19–21]. By contrast, theoretical studies on cell growth during solid-state nanofoaming are limited. Costeux and co-workers [16,22] have simulated void nucleation and void growth during the solid-state nanofoaming of acrylate co-polymers by making use of the model of Shafi *et al.* [23]. However, their model overestimates the final porosity of their nanofoams. The mismatch between the simulated and measured porosity of acrylic nanofoams may be due to (i) the assumption that cell growth continues until the foaming temperature attains the glass transition temperature of the polymer-gas solid and/or (ii) the assumption that the polymer-gas solid surrounding the cell is in a liquid (viscous) state throughout the solid-state foaming process. In reality, void growth occurs at temperatures close to the glass transition temperature of the solid surrounding the void, and significantly below the melting temperature. This is addressed in detail in the present study.

(a) Scope of study

Nanofoams are produced from two PMMA grades of widely different molecular weight; a solid-state foaming process is used with CO_2 as the blowing agent. We characterize the microstructure of the nanofoams in terms of porosity f, cell size l and cell nucleation density N_d. In addition, we develop a void growth model, based on the constitutive law of PMMA grades close to the glass transition temperature, by building on the recent study of Van Loock & Fleck [24]. Both predicted and measured final porosities are obtained as a function of foaming time and foaming temperature; also, cell wall tearing mechanisms are considered in order to account for the observed limit in final porosity.

2. Nanofoaming experiments

(a) Materials

Foaming experiments were conducted on two PMMA grades: pelletized PMMA (Altuglas V825T) of average molecular weight[1] $M_w = 92\,500\,\mathrm{g\,mol^{-1}}$ and cast PMMA sheets (Altuglas CN with sheet thickness close to 3 mm) of high molecular weight $M_w = 3\,580\,000\,\mathrm{g\,mol^{-1}}$. We shall refer to the Altuglas V825T and Altuglas CN grades as 'low M_w PMMA' and 'high M_w PMMA', respectively. Both grades have a density $\rho^p = 1190\,\mathrm{kg\,m^{-3}}$ (as measured at 23°C and at 50% relative humidity). The glass transition temperatures $T_g = 114.5$°C of the low M_w PMMA, and $T_g = 116.5$°C of the high M_w PMMA, have been measured by differential scanning calorimetry (DSC) using a heating rate of $10\,^{\circ}\mathrm{C\,min^{-1}}$: the values are almost equal.

(b) Solid-state nanofoaming experiments

Foaming precursors of the low M_w and high M_w PMMA grades were made as follows. The low M_w PMMA pellets were heated to 250°C for 450 s and then compressed for 60 s between two heated plates at a pressure equal to 17 MPa. The resulting sheet was cooled to room temperature with the pressure of 17 MPa maintained. Cuboid precursors of dimension $20 \times 10 \times 3\,\mathrm{mm^3}$ were machined from the low M_w PMMA sheet and from the as-received high M_w PMMA sheet.

Foaming experiments were performed in a pressure vessel[2] with feedback pressure controller[3] and temperature controller.[4] Medical grade CO_2 (greater than 99.9% purity) was used as the blowing agent for the foaming experiments. The solid-state foaming process involved a nucleation step and then a subsequent growth step, as detailed by Martin-de León *et al.* [9].

[1]The average molecular weight was measured by gas permeation chromatography (GPC) with an Agilent Technologies PL GPC220 (USA) instrument with a nominal flow rate equal to $1.67 \times 10^{-5}\,\mathrm{l\,s^{-1}}$ at a test temperature equal to 30°C.

[2]Pressure vessel model PARR 4681 of Parr Instrument Company (USA).

[3]Pressure controller pump SFT-10 of Supercritical Fluid Technologies Inc (USA).

[4]Temperature controller CAL 3300 of CAL Controls Ltd (UK).

First, the precursor samples were held in the pressure vessel at a constant CO_2 saturation pressure equal to 31 MPa, and at a constant temperature equal to 25°C for 24 h in order to ensure saturation of the CO_2 into the PMMA. The mass concentration[5] C, at equilibrium, is close to 24 wt% for both the low and high M_w PMMA, by making use of the measurement procedure of Martin-de León *et al.* [9]. Second, the pressure was released to atmospheric pressure at the rapid rate of 100 MPa s^{-1}; this is the *nucleation* step. Third, samples were foamed in a foaming bath[6] at selected foaming temperatures (25°C, 40°C, 60°C, 80°C, 100°C) and selected foaming times[7] (60 s, 180 s, 300 s, 600 s); this is the void *growth* step. It is assumed throughout the remainder of this study that the foaming times are sufficiently long for the temperature to be spatially uniform[8] within the sample.

(c) Characterization of the PMMA nanofoams

(i) Porosity

The density ρ^f of the foamed samples was determined by the water-displacement method with a weight balance.[9] A surface layer of depth 200 µm was removed by polishing[10] to ensure that the solid skin (of thickness below 100 µm) was absent before the density measurements were made. The porosity f of the samples is obtained by

$$f = 1 - \frac{\rho^f}{\rho^p}, \tag{2.1}$$

where ρ^p ($= 1\,190\ \mathrm{kg\,m^{-3}}$) is the density of solid PMMA.

(ii) Microstructure

Foamed samples were cooled in liquid nitrogen and then fractured. The fracture surfaces were coated with a layer of gold by sputtering,[11] and micrographs of the coated fracture surfaces were taken by a scanning electron microscope[12] (SEM). The cellular structure of each material was characterized by analysing the micrographs with dedicated in-house software based on ImageJ/FIJI [26]. Microstructural parameters such as the average cell size l, standard deviation s of the observed cell sizes, and cell nucleation density N_d, using the method as suggested by Kumar & Suh [27], were obtained.[13]

(iii) Open cell content

The open cell content of the foamed samples was measured by gas pycnometry[14] with nitrogen in accordance with the ASTM D6226-15 standard [28]. The open cell content ratio O_v is defined

[5]We define the mass concentration C of CO_2 in PMMA with respect to the total mass of the PMMA–CO_2 mixture. Note that the definition of CO_2 solubility (with respect to the mass of the PMMA absent CO_2) is used in the work of Martin-de León *et al.* [9].

[6]Thermal bath J.P. Selecta Model 6000685 of Grupo Selecta (Spain). The time between the pressure release and the start of foaming was close to 120 s.

[7]Samples were immersed in a water bath at a temperature close to 10°C at the end of the foaming time.

[8]The justification for this assumption is as follows. Immersion of the sample in water or oil provides excellent heat transfer at the surface of the sample. The time constant $\tau = x^2/\kappa \approx 20$ s, where $x = 1.5$ mm is the half-thickness of the PMMA sample and $\kappa = 1.1 \times 10^{-7}\ \mathrm{m^2\,s^{-1}}$ is the thermal diffusivity of PMMA at room temperature [25].

[9]Analytical balance AT261 of Mettler-Toledo (USA).

[10]Grinding and polishing system LaboPOl2-LaboForce3 of Struers (USA).

[11]Sputter coater SDC 005 of Balzers Union (Liechtenstein).

[12]Scanning electron microscope QUANTA 200 FEG of Thermo Fisher Scientific (USA).

[13]At least 200 cells were analysed from multiple micrographs per foamed sample.

[14]Gas pycnometer (USA) AccuPyc II 1340 of Micromeritics (USA).

as the ratio of the volume of open pores to the total pore volume of a foam, and is obtained by

$$O_v = \frac{V^g - V^p - V^s}{fV^g}, \tag{2.2}$$

where V^g is the geometric volume of the foam, V^p is the pycnometer volume and V^s is a penalty volume to account for the volume of the cells at the surface of the foam. The penalty volume V^s is assumed to be close to zero in the case of nanofoams. The geometric volume V^g is measured by the water-displacement method as detailed above. Foamed samples were subjected to a pressure scan from 0.02 to 0.13 MPa in the gas pycnometer. The pycnometer volume initially decreases as the gas pressure increases until the interconnected open cells are completely filled with gas and the pycnometer volume remains constant at increased pressures. We take this constant value of pycnometer volume V^p in order to calculate O_v via equation (2.2).

3. Results of the nanofoaming experiments

The measured porosity f, average observed cell size l, standard deviation s of observed cell sizes and cell nucleation density N_d of the nanofoams are reported in tables 1 and 2 for the low M_w and high M_w grades of PMMA, respectively. In addition, a representative series of SEM micrographs of the nanofoams is shown in figure 2. The low M_w and the high M_w nanofoams have contrasting microstructures and the cell nucleation density of the low M_w nanofoams ($N_d \approx 2 \times 10^{20}$ m^{-3}) is an order of magnitude less than that of the high M_w nanofoams ($N_d \approx 2 \times 10^{21}$ m^{-3}). The average cell size l of the high M_w nanofoams ranges from 20 to 50 nm, and is an order of magnitude smaller than the average cell size of the low M_w nanofoams (of size 200–350 nm). These values of l and N_d for the low M_w nanofoams are consistent with the results of Martin-de León *et al.* [9], who conducted solid-state foaming experiments with an identical low M_w PMMA grade. The measured average cell size l of the low M_w and the high M_w nanofoams, as a function of foaming time t_f for $T_f = 60$°C, is plotted in figure 3*a*. Void growth typically occurs over a foaming time period of 60–180 s, followed by arrest. There is a mild dependence of the foaming temperature T_f upon the final value for l (tables 1 and 2).

The measured porosity f of the nanofoams is plotted as a function of t_f in figure 3*b* for $T_f = 60$°C and for $T_f = 100$°C. Consistent with the l versus t_f curves for $T_f = 60$°C, as presented in figure 3*a*, the porosity increases over a foaming period of 60–180 s until a stable (t_f-independent) value of final porosity is achieved. The highest observed porosity of the low M_w PMMA nanofoams ($f_{max} = 0.75$) is approximately 25% higher than that of the high M_w PMMA nanofoams ($f_{max} = 0.60$). At a foaming temperature of $T_f = 100$°C, the porosity decreases with increasing foaming time beyond $t_f = 60$ s, and this is due to collapse of the foamed structure. This behaviour is also illustrated in plots of f versus T_f, over the explored range of foaming times; see figure 3*c*,*d* for the low M_w and high M_w PMMA nanofoams, respectively.

The measured open cell content O_v is plotted as a function of the measured porosity f in figure 4*a* (low M_w) and in figure 4*b* (high M_w) for 20°C $\leq T_f \leq$ 80°C. Nanofoams with porosities well below the highest observed porosity f_{max} are closed-cell in nature. An abrupt transition to an open-celled structure occurs close to f_{max}. The observed collapse of the foam at $T_f = 100$°C is preceded by cell wall rupture for the low M_w nanofoams (figure 2*b*) and by the formation of cracks interconnecting the nano-sized pores for the high M_w nanofoams (figure 2*d*).

4. Void growth model

A void growth model is now developed to predict porosity as a function of foaming time and foaming temperature for the PMMA nanofoams. The expansion of a pre-existing as-nucleated spherical cavity during solid-state nanofoaming is simulated by means of a one-dimensional single-cell growth model [20,29]. A finite shell surrounds the spherical void in order to account for void–void interaction in an approximate manner. More sophisticated models of an array of voids

Table 1. Measured porosity f, average cell size l, standard deviation of observed cell size s, cell nucleation density N_d and open cell content O_v of the low M_w PMMA nanofoams as a function of foaming time t_f and foaming temperature T_f. Foams collapsed at $T_f = 100°C$, and so no open cell content values are reported for nanofoams produced at $T_f = 100°C$.

t_f (s)	T_f (°C)	f	l (nm)	s (nm)	N_d (10^{20} m^{-3})	O_v
60	25	0.45	219	87	1.50	0.12
180	25	0.47	228	79	1.50	0.08
300	25	0.51	283	112	0.91	0.08
600	25	0.51	235	85	1.48	0.08
60	40	0.52	262	102	1.22	0.07
180	40	0.61	250	125	1.70	0.02
300	40	0.64	254	105	1.27	0.15
600	40	0.66	233	103	2.11	0.14
60	60	0.56	234	89	2.34	0.07
180	60	0.66	297	111	1.72	0.33
300	60	0.68	279	122	1.76	0.40
600	60	0.68	284	109	1.63	0.36
60	80	0.72	333	134	1.16	0.63
180	80	0.74	288	138	1.83	0.90
300	80	0.75	297	125	1.75	0.78
600	80	0.73	274	109	2.08	0.93
60	100	0.64	297	122	1.21	—
180	100	0.68	253	110	1.81	—
300	100	0.62	246	103	1.75	—
600	100	0.51	291	125	0.76	—

(such as periodic cell models) could be adopted but the intent here is to emphasize the strong role of the evolving constitutive response of the cell wall.

Consider a polymer-gas solid with equi-sized spherical voids. A cross section of the undeformed (reference) configuration of the spherical void, with initial radius a_0 and initial outer radius b_0, along with the adopted spherical coordinate system (r, θ, ϕ), is shown in figure 5. Assume that the initial gas pressure p_0 in the as-nucleated void equals the saturation pressure during the saturation phase prior to nucleation of the voids. The deformed configuration for the void of inner radius a and outer radius b at time t is shown in figure 5.

(a) Kinematics

Assume that the void remains spherical during growth and that the solid surrounding the void is incompressible. Then a material point within the cell wall, initially at radius R, is displaced to a radius r such that

$$r^3 - a^3 = R^3 - a_0^3, \tag{4.1}$$

by incompressibility. For later use, this relation is rearranged to the form

$$\left(\frac{r}{R}\right)^3 = 1 + \left(\frac{a_0}{R}\right)^3 \left[\left(\frac{a}{a_0}\right)^3 - 1\right]. \tag{4.2}$$

Table 2. Measured values for the porosity f, the average observed cell size l, the standard deviation of the observed cell size s, the cell nucleation density N_d, and the open cell content O_v of the high M_w PMMA nanofoams as a function of foaming time t_f and foaming temperature T_f. Foams collapsed at $T_f = 100°C$, and so no open cell content values are reported for the nanofoams produced at $T_f = 100°C$.

t_f (s)	T_f (°C)	f	l (nm)	s (nm)	N_d (10^{20} m^{-3})	O_v
60	25	0.22	36	14	14.9	0.30
180	25	0.28	23	10	40.0	0.22
300	25	0.29	30	12	9.0	0.28
600	25	0.31	36	18	6.9	0.21
60	40	0.33	28	13	54.2	0.19
180	40	0.42	32	16	32.3	0.07
300	40	0.45	37	14	7.8	0.08
600	40	0.47	45	29	26.0	0.09
60	60	0.45	37	14	20.4	0.08
180	60	0.55	39	17	24.0	0.03
300	60	0.57	40	17	31.8	0.28
600	60	0.57	41	19	25.8	0.03
60	80	0.58	39	20	21.8	0.51
180	80	0.60	39	19	27.8	0.73
300	80	0.60	38	19	36.6	0.95
600	80	0.59	44	22	46.6	0.88
60	100	0.59	34	15	35.4	—
180	100	0.53	27	14	80.4	—
300	100	0.50	37	18	24.9	—
600	100	0.45	34	12	32.6	—

Note that r/R is a function of the *time-like variable* (a/a_0) and of the Lagrangian position variable R/a_0. The von Mises effective strain ε_e is defined in the usual manner as $\varepsilon_e^2 = (2/3)\varepsilon_{ij}\varepsilon_{ij}$, giving

$$\varepsilon_e = |2\varepsilon_{\theta\theta}| = 2\ln\left(\frac{r}{R}\right), \tag{4.3}$$

where $\varepsilon_{\theta\theta}$ is the hoop strain. Now insert equation (4.2) into equation (4.3) to obtain

$$\varepsilon_e = \frac{2}{3}\ln\left[1 + \left(\frac{a_0}{R}\right)^3\left(\left(\frac{a}{a_0}\right)^3 - 1\right)\right] \tag{4.4}$$

and take the time derivative of r in equation (4.1) to give

$$\dot{r} = v_r = \left(\frac{a}{r}\right)^2\dot{a}, \tag{4.5}$$

where v_r is the radial velocity of a material element at r. Consequently, the effective strain rate $\dot{\varepsilon}_e$ reads

$$\dot{\varepsilon}_e = \left|\frac{\partial v_r}{\partial r}\right| = \frac{2a^2}{R^3}\left(\frac{r}{R}\right)^{-3}\dot{a}. \tag{4.6}$$

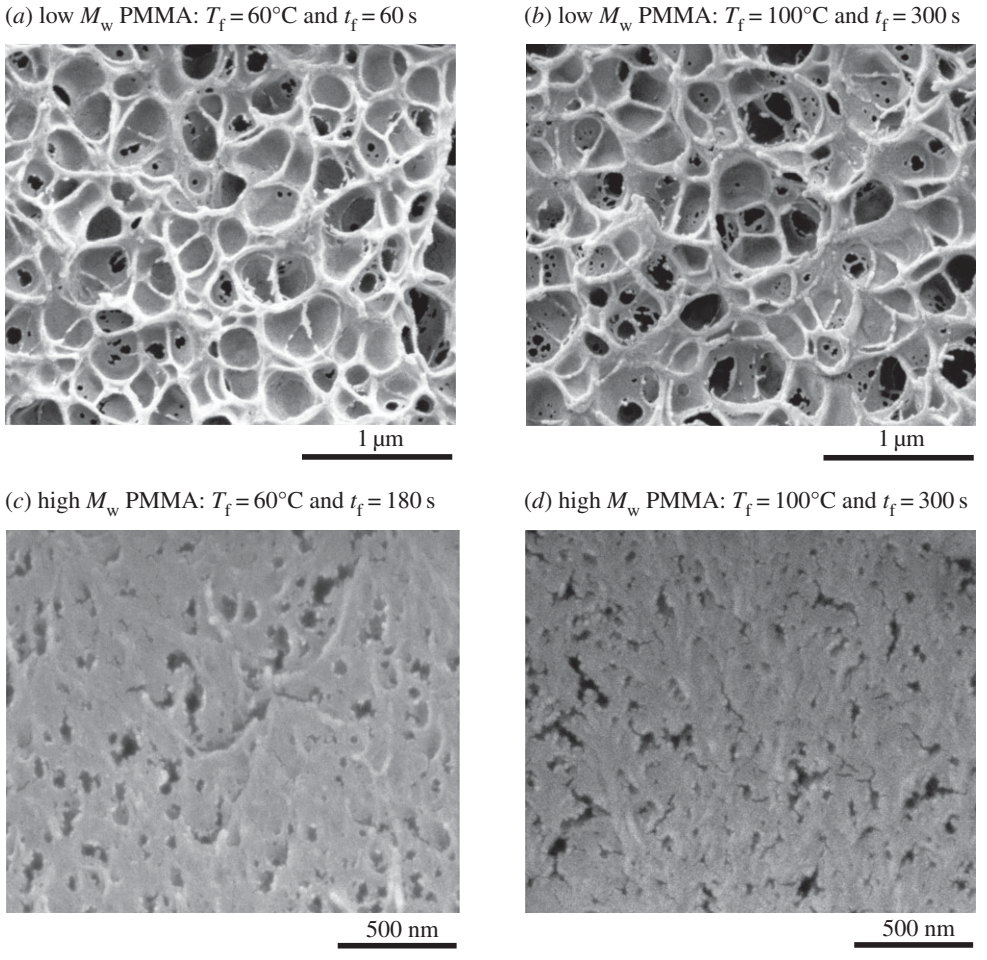

Figure 2. SEM micrographs of the low M_w nanofoams at (*a*) $T_f = 60°C$, (*b*) $T_f = 100°C$ and of the high M_w nanofoams at (*c*) $T_f = 60°C$ and (*d*) $T_f = 100°C$.

(b) Equilibrium

Write $(\sigma_{rr}, \sigma_{\theta\theta}, \sigma_{\phi\phi})$ as the active stress components in the spherical coordinate system. Radial equilibrium dictates that [30]

$$\frac{\partial \sigma_{rr}}{\partial r} + \frac{1}{r}(2\sigma_{rr} - \sigma_{\theta\theta} - \sigma_{\phi\phi}) = 0. \tag{4.7}$$

Due to symmetry, $\sigma_{\phi\phi} = \sigma_{\theta\theta}$ and equation (4.7) simplifies to

$$\frac{\partial \sigma_{rr}}{\partial r} = \frac{2(\sigma_{\theta\theta} - \sigma_{rr})}{r} = \frac{2\sigma_e}{r}, \tag{4.8}$$

where $\sigma_e = \sigma_{\theta\theta} - \sigma_{rr}$ is the von Mises effective stress [31]. Integration of equation (4.8) provides the gas pressure p inside the cavity as an implicit function of current void radius a, and ambient pressure p_a such that

$$p - p_a = \int_{r=b}^{r=a} \frac{2\sigma_e}{r} \mathrm{d}r. \tag{4.9}$$

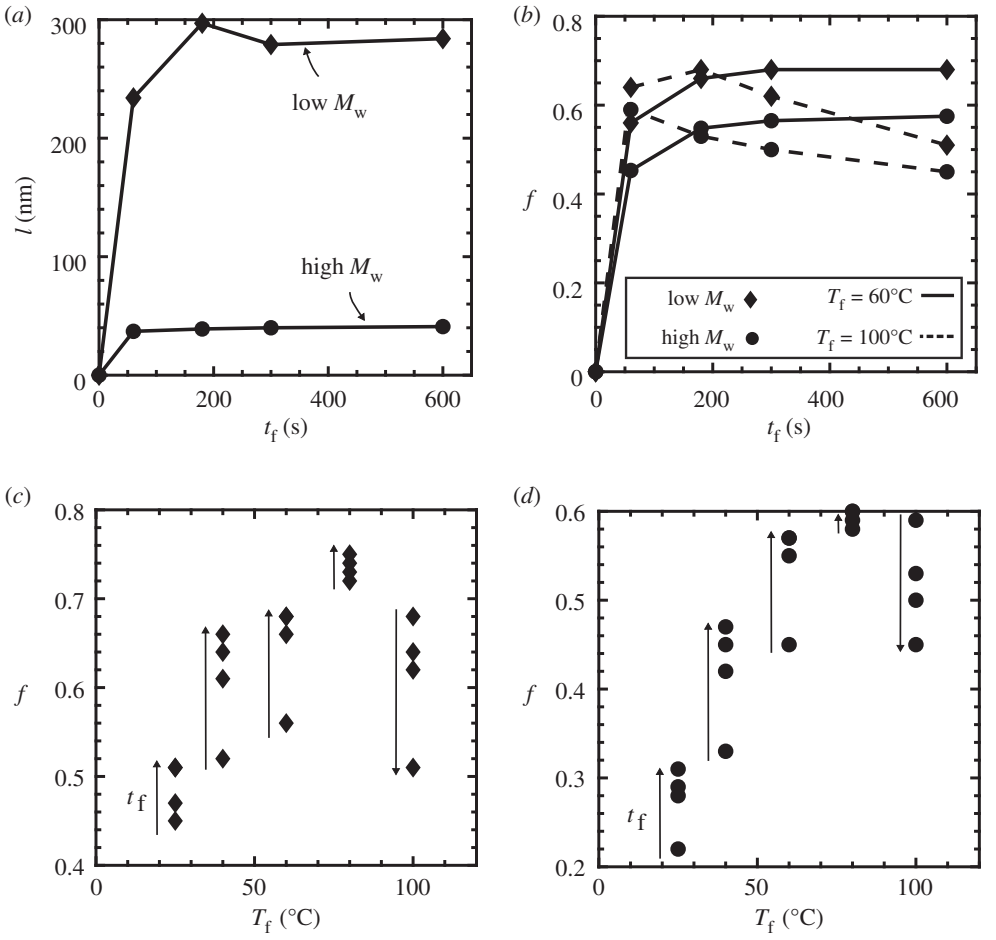

Figure 3. Nanofoaming experiments on the low M_w and high M_w PMMA grades: (*a*) measured average cell size *l* versus foaming time t_f for $T_f = 60°C$, (*b*) measured porosity *f* versus foaming time t_f for $T_f = 60°C$ and $T_f = 100°C$, (*c*) measured porosity *f* versus foaming temperature T_f for the range of explored foaming times ($t_f = 60–600$ s) for the low M_w nanofoams and (*d*) measured *f* versus T_f for the range of explored foaming times ($t_f = 60–600$ s) for the high M_w nanofoams.

Now make use of equation (4.1) to re-express the above integral in the form

$$p - p_a = \int_{R=b_0}^{R=a_0} \frac{2}{R}\left(\frac{R}{r}\right)^3 \sigma_e \mathrm{d}R. \tag{4.10}$$

The effective stress σ_e is a function of the effective strain ε_e, the effective strain rate $\dot{\varepsilon}_e$, as given by equation (4.6) and the normalized temperature T/T_g via the constitutive law for the PMMA–CO_2 solid, of general functional form *F* where

$$\sigma_e = F\left(\varepsilon_e, \dot{\varepsilon}_e, \frac{T}{T_g}\right). \tag{4.11}$$

The choice of *F* is given below. We show in appendix A that the concentration *C* of CO_2 can be taken to be spatially uniform throughout the spherical shell at any instant of time, but the magnitude of *C* depends upon the current size of the void by a mass conservation argument as detailed below. This leads to a major simplification of the analysis. The glass transition temperature T_g of the PMMA is taken to be a function of CO_2 concentration *C*, and is also given below.

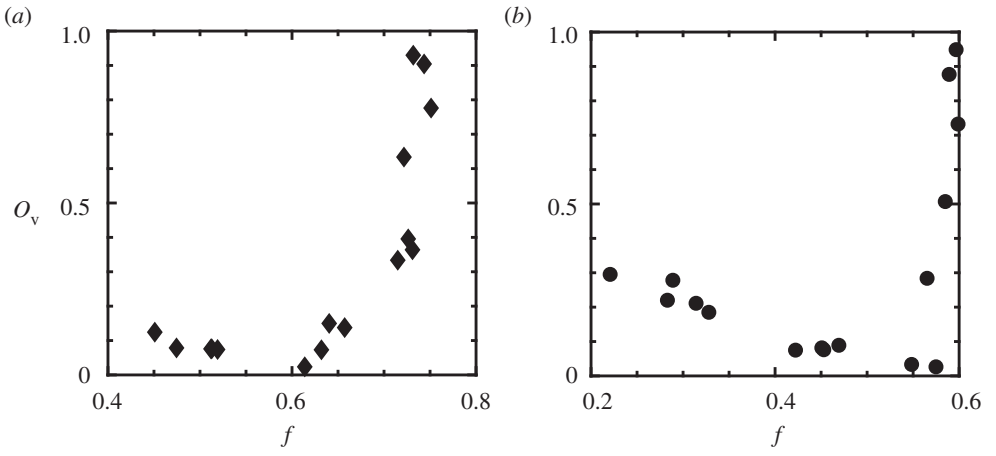

Figure 4. Measured open cell content O_v as a function of porosity f for (*a*) the low M_w PMMA nanofoam and (*b*) high M_w PMMA nanofoam.

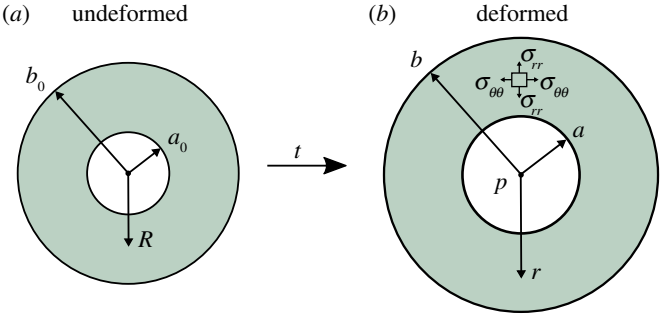

Figure 5. Spherical void in (*a*) undeformed configuration with initial radius a_0 and initial outer radius b_0 and (*b*) deformed configuration at time t of the void with radius a, outer radius b and gas pressure p. (Online version in colour.)

(c) The solution strategy

Substitute equation (4.11) into (4.10), and integrate over the thickness of the spherical shell in order to obtain an expression for the gas pressure p within the cavity as a function of $\dot{a}$ (via equation (4.6)), and the current state, as parametrized by the current value of a/a_0. It remains to obtain an expression for p as a function of a/a_0 by considering the gas law for the void and mass conservation of CO_2 in the void and solid PMMA. Once we have obtained p as a function of a/a_0, we can re-express equation (4.10) as $\dot{a}$ as a function of a/a_0; integration of $\dot{a}$ then gives the time evolution of a/a_0.

(d) Gas laws

The equilibrium concentration C of CO_2 in PMMA is a function of CO_2 pressure p and of temperature. Here, we assume that Henry's Law suffices such that [32–35]

$$C = K_H p, \tag{4.12}$$

where Henry's Law coefficient K_H is assumed to be independent of both temperature and pressure. Assume that the concentration of CO_2 at the surface of the cavity ($R = a_0$) is in equilibrium with the CO_2 pressure within the void via equation (4.12).

Take $K_H = 7.8 \times 10^{-9}\,\mathrm{Pa}^{-1}$ for both the low M_w and the M_w PMMA grades, based on the measured $C = 0.24$ equilibrium concentration of CO_2 in PMMA at a pressure $p = 31$ MPa and temperature $T = 25°C$, as detailed in §2b. Also, assume that the CO_2 gas in the void satisfies the ideal gas law

$$p = \frac{\rho^g RT}{M_w^g}, \tag{4.13}$$

where R is the universal gas constant.

It is recognized that the use of Henry's Law and the ideal gas law have a somewhat limited range of validity and the current analysis can be embellished by employing alternative laws such as the lattice-based theory equation of state of Sanchez & Lacombe [36–39] or empirical non-ideal equation of states for CO_2 [40,41]. However, the use of a number of such laws is considered to lie beyond the scope of the present study.

(e) Mass conservation

We shall assume that the total mass of gas molecules in the voids and in the surrounding solid is constant; leakage of gas molecules to neighbouring voids or the sample's environment is neglected. Also, assume that the concentration C of dissolved CO_2 in the PMMA spherical shell is independent of radius, as justified in appendix A. The resulting mass conservation statement for CO_2 reads

$$C\rho^p(b^3 - a^3) + \rho^g a^3 = C_0\rho^p(b_0^3 - a_0^3) + \rho_0^g a_0^3, \tag{4.14}$$

where ρ^p is the density[15] of the PMMA–CO_2 solid and ρ^g is the density of the CO_2 in the voids. Substitution of equation (4.13) into equation (4.14) gives p as a function of cavity size a/a_0.

(f) Dependence of the glass transition temperature of PMMA upon CO_2 content

The dissolution of CO_2 into a linear, amorphous polymer such as PMMA reduces the glass transition temperature T_g of the PMMA–CO_2 solid. This plasticization effect is attributed to the increased mobility of PMMA chains due to lubrication by the CO_2 molecules, and the decrease of the intermolecular bond strength as the CO_2 molecules increase the spacing between the PMMA chains [42,43]. A range of experimental techniques has been used in the literature to determine the glass transition temperature T_g of PMMA as a function of CO_2 mass concentration C. Chiou *et al.* [44] made use of DSC to measure T_g/T_g^0 as a function of C, where $T_g^0 = T_g(C = 0)$. Likewise, Wissinger & Paulaitis [45] measured the dependence of T_g/T_g^0 upon C via creep compliance measurements. Guo & Kumar [46] made use of solid-state foaming experiments to observe the relationship between T_g/T_g^0 and CO_2 for a PMMA–CO_2 mixture. The measured T_g/T_g^0 versus C data, for PMMA–CO_2, as reported by Chiou *et al.* [44], Wissinger & Paulaitis [45] and Guo & Kumar [46] are shown in figure 6. Chow [47] used statistical thermodynamics to predict T_g/T_g^0 as a function of C and introduced a parameter θ where

$$\theta = \frac{M_w^p}{zM_w^g}\frac{C}{1 - C}. \tag{4.15}$$

Here, M_w^p is the molecular weight of the polymer repeat unit ($M_w^p = 100.12\,\mathrm{g\,mol}^{-1}$ for a methyl methacrylate monomer), M_w^g is the molecular weight of the gas ($M_w^g = 44.01\,\mathrm{g\,mol}^{-1}$ for CO_2), and z is a lattice coordination number equal to 2, as suggested by Chow [47]. In addition, Chow [47] defined a parameter β

$$\beta = \frac{zR}{M_w^p \Delta C_p}, \tag{4.16}$$

where ΔC_p is the change in specific heat capacity of the polymer at the glass transition temperature at constant pressure. The normalized glass transition temperature is then predicted

[15]We assume that the density of the PMMA–CO_2 solid is equal to the density of PMMA absent CO_2 at standard conditions (i.e. $\rho^p = 1190\,\mathrm{kg\,m}^{-3}$) based on the measurements of Pantoula & Panayiotou [33] and Pantoula *et al.* [34] who observed that the relative increase in volume of a PMMA–CO_2 mixture is close to the relative increase of the mass of a PMMA–CO_2 mixture for a CO_2 pressure up to 30 MPa.

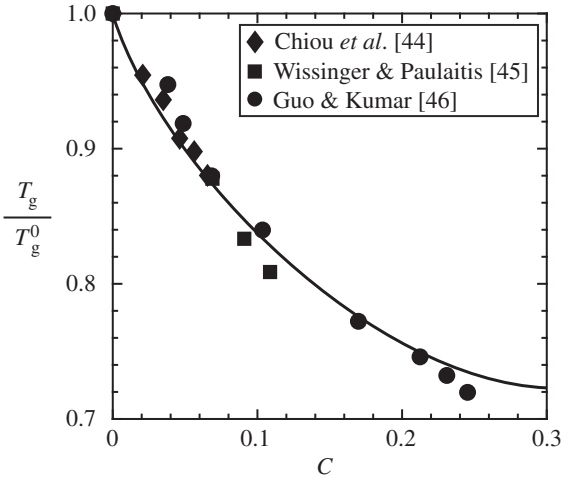

Figure 6. The normalized glass transition temperature T_g/T_g^0 of PMMA as a function of CO_2 mass concentration C, as reported by Chiou *et al.* [44], Wissinger & Paulaitis [45] and Guo & Kumar [46]. The T_g/T_g^0 versus C curve is given by the calibrated version of equation (4.17).

by

$$\frac{T_g}{T_g^0} = \exp[\beta((1-\theta)\ln(1-\theta) + \theta\ln\theta)]. \tag{4.17}$$

The above equation is curve fitted to the measured T_g/T_g^0 versus C data shown in figure 6 by a suitable choice of ΔC_p. The fitted value for $\Delta C_p = 355\ \mathrm{J\,kg^{-1}K^{-1}}$ which is slightly higher than the value of ΔC_p for PMMA as measured by DSC [44,48]. We note in passing that the value of $\Delta C_p = 355\ \mathrm{J\,kg^{-1}\,K^{-1}}$ gives a good fit to the data of Guo & Kumar [46] in addition to the data of by Chiou *et al.* [44] and Wissinger & Paulaitis [45] (figure 6). This is consistent with the observation by Guo & Kumar [46] that a value of $\Delta C_p = 265\ \mathrm{J\,kg^{-1}\,K^{-1}}$ (assuming $z = 2$) gives a relatively poor fit to their data.

(g) Constitutive model for the PMMA–CO_2 solid

We assume that the effective stress σ_e of the PMMA–CO_2 solid at a given strain ε_e, strain rate $\dot{\varepsilon}_e$ and normalized temperature T/T_g is the same as that given by PMMA in the absence of CO_2: the effect of CO_2 is accounted for by a shift in the value for T_g. The deformation mechanisms for PMMA in uniaxial tension close to the glass transition temperature have been reviewed recently by Van Loock & Fleck [24] and deformation mechanism maps were constructed by performing a series of uniaxial tension tests on the high M_w PMMA over a range of temperatures near the glass transition and over two decades of strain rate. The operative deformation mechanism depends upon the temperature T/T_g, the strain rate $\dot{\varepsilon}_e$ and strain ε_e. We shall make use of the constitutive models as calibrated by Van Loock & Fleck [24] for the high M_w PMMA: the Ree–Eyring equation and a rubbery-flow model. For the low M_w PMMA, it is necessary to construct an alternative deformation mechanism map. This is reported in appendix B. For this grade, the relevant deformation mechanisms are Ree–Eyring and viscous flow.

The Ree–Eyring equation relates σ_e in the glassy and glass transition regime to temperature T/T_g and strain rate $\dot{\varepsilon}_e$

$$\frac{\dot{\varepsilon}_e}{\dot{\varepsilon}_0} = \sinh\left(\frac{\sigma_e v}{kT}\right)\exp\left(\frac{-q}{kT}\right), \tag{4.18}$$

where $\dot{\varepsilon}_0$ is a reference strain rate, q is an activation energy, v is an activation volume and k is Boltzmann's constant. Visco-elastic effects are neglected in this finite strain regime. Van Loock &

Table 3. Fitted parameters for the constitutive laws for the low M_w PMMA (equations (4.18) and (4.20)) and the high M_w PMMA obtained from Van Loock & Fleck [24], see equations (4.18) and (4.19).

	low M_w PMMA	high M_w PMMA
v (nm^{-3})	2.5	1.8
q (J)	7.31×10^{-19}	7.31×10^{-19}
$\dot{\varepsilon}_0$ (s^{-1})	1.5×10^{56}	1.5×10^{56}
η_0 (Pa s)	2.8×10^{6}	—
C_1	3.2	—
C_2 (K)	17.3	—
E_R^0 (MPa)	—	65.8
α_R	—	0.8
$\dot{\varepsilon}_R$ (s^{-1})	—	1.58
n	—	0.173

Fleck [24] also fitted an empirical equation to relate σ_e to T/T_g, ε_e and $\dot{\varepsilon}_e$ in the rubbery regime for the high M_w PMMA

$$\sigma_e = E_0 \left(1 - \alpha_R \frac{T}{T_g}\right) \left(\frac{\dot{\varepsilon}_e}{\dot{\varepsilon}_R}\right)^n \varepsilon_e, \tag{4.19}$$

where E_0 is a reference modulus, α_R is a temperature sensitivity coefficient, $\dot{\varepsilon}_R$ a reference strain rate, and n a strain rate sensitivity coefficient.

Note that the rubbery regime above the glass transition is absent for PMMA grades of relatively low molecular weight, i.e. $M_w < 150$ kg mol^{-1} [49]. Instead, a linear, viscous flow rule can be used to describe the constitutive behaviour of a low M_w PMMA for $T/T_g \gg 1$

$$\sigma_e = 3\eta\dot{\varepsilon}_e, \tag{4.20}$$

where η is a temperature-dependent viscosity [50,51]

$$\eta = \eta_0 \exp\left(\frac{-C_1(T/T_g - 1)}{C_2/T_g + T/T_g - 1}\right), \tag{4.21}$$

in terms of a reference viscosity η_0 at $T/T_g = 1$; C_1 and C_2 are fitting constants.

The dependence of the effective stress σ_e upon normalized temperature T/T_g and strain rate $\dot{\varepsilon}_e$ is assumed to be governed by equations (4.18) and (4.19) for the high M_w PMMA and by equations (4.18) and (4.20) for the low M_w PMMA. The fitted parameters for the constitutive laws for the high M_w PMMA are taken from Van Loock & Fleck[16] [24] and are summarized in table 3. An additional series of tensile tests have been performed on the low M_w PMMA at temperatures close to the glass transition in order to calibrate equations (4.18) and (4.20) for the low M_w PMMA as detailed in appendix B. The resulting calibrated parameters for equations (4.18) and (4.20) for the low M_w PMMA are included in table 3.

(h) Temperature-time profile during void growth

During the rapid release of pressure at the end of the saturation phase, the samples cool down from the saturation temperature equal to 25°C to a temperature[17] $T_0 = -15$°C due to adiabatic

[16]We assume that the dependence of the effective stress σ_e of the PMMA–CO_2 solid upon pressure is small as a first-order approximation for the void growth problem.

[17]Measured by placing a thermocouple on the sample after pressure release at the end of the saturation phase.

Table 4. Summary of the assumed processing parameters and material properties for the void growth predictions.

	low M_w PMMA	high M_w PMMA
p_0 (MPa)	31	31
p_a (MPa)	0.1	0.1
τ (s)	20	20
ρ^p (kg m^{-3})	1190	1190
T_g (°C)	114.5	116.5
f_0	10^{-3}	10^{-3}
a_0 (nm)	10.5	5

cooling of the expanding gas. The samples are subsequently placed in a thermal bath at a maintained foaming temperature T_f. Upon submersion in the foaming bath, assume that the temperature profile $T(t)$ is of the form

$$T = T_0 + (T_f - T_0)\left(1 - \exp\left(\frac{-t}{\tau}\right)\right), \tag{4.22}$$

where τ is a time constant associated with the heat conduction into the PMMA, as measured by a thermocouple. The direct measurement of the temperature history by an *in situ* thermocouple supports this simple relation. This expression also agrees with the dominant, leading-order term in the series expansion of the temperature dependence for a cuboid with a sudden jump in surface temperature; see, for example, Carslaw & Jaeger [52].

(i) Void growth simulations

Void growth during solid-state foaming is simulated by solving the equilibrium equation, equation (4.10), and the mass conservation statement, equation (4.14), simultaneously, with due account of the dependence of T_g upon C via equation (4.17), the dependence of the effective stress σ_e of the PMMA–CO_2 solid upon ε_e, $\dot{\varepsilon}_e$ and T/T_g via equations (4.18)–(4.20), the gas laws via equations (4.12) and (4.13), and the time-temperature profile as captured by equation (4.22). The resulting system of equations is solved by numerical integration.[18] The values of the processing parameters and the material properties are summarized in table 4. Note that the initial porosity f_0 is

$$f_0 = \left(\frac{a_0}{b_0}\right)^3, \tag{4.23}$$

and is estimated[19] to equal 10^{-3} for both the low M_w and high M_w PMMA nanofoams. The initial void radius a_0 is estimated by

$$a_0 \approx \left(\frac{3f_0}{4\pi N_d}\right)^{1/3}, \tag{4.24}$$

where the cell nucleation density $N_d = 2 \times 10^{20}$ m^{-3} for the low M_w PMMA nanofoams (table 1) and $N_d = 20 \times 10^{20}$ m^{-3} for the high M_w PMMA nanofoams (table 2).

[18]The numerical integration was conducted within the Matlab computing environment by means of the *ode15s* function.

[19]The initial porosity f_0 is estimated by saturating low M_w and high M_w PMMA precursors with CO_2 at $p = 31$ MPa and $T = 25$°C. Upon release of the pressure to atmospheric pressure, the samples were immediately immersed in liquid nitrogen to prevent the growth of the nucleated voids. The porosity of the samples was measured by the method detailed in §2 after the CO_2 was completely desorbed. The measured porosity was assumed to be representative for f_0.

5. Results and discussion of the void growth predictions

Consider the deformation mechanism maps for the low M_w PMMA (figure 7*a*) and for the high M_w PMMA (figure 7*b*). We superpose the predicted trajectory of the effective stress at the surface of the cavity σ_e by the void growth model as a function of T/T_g for foaming temperatures $T_f = 25°C$ and $T_f = 80°C$, and for a foaming time up to 600 s. Note that both the temperature T and glass transition temperature T_g evolve in time during foaming. For both the low M_w and high M_w PMMA, at the start of foaming, $T = T_0$ and T/T_g is close to 0.9; at this instant σ_e is close to 0.8 MPa for the low M_w PMMA and σ_e is close to 0.3 MPa for the high M_w PMMA. When the temperature increases from $T = T_0$ to $T = T_f$, T/T_g rises to almost unity and σ_e rises steeply. The void growth simulations suggest that during solid-state foaming of PMMA, the normalized temperature T/T_g remains between 0.9 and 1 and consequently void growth does not occur within either the viscous regime (low M_w PMMA) or within the rubbery regime (high M_w PMMA).

The measured porosity f is plotted as a function of foaming time t_f for $T_f = 25°C$ to $T_f = 80°C$, and compared with the predicted f versus t_f curves for the low M_w and high M_w nanofoams, in figure 8*a*,*b*, respectively. There is reasonably good agreement between the measured and the predicted f–t_f curves for $T_f = 25°C$ and $T_f = 40°C$. The void growth model overestimates the porosity at $T_f = 60°C$ and at $T_f = 80°C$, where porosities close to f_{max} are observed. Observations of SEM micrographs suggest that cell walls tear, leading to open-celled microstructures. This is confirmed by open cell content measurements using gas pycnometry: nanofoams with the highest observed porosities have predominantly open-celled microstructures (figure 4). At increased foaming temperatures (i.e. $T_f = 100°C$) collapse of the foamed open-celled microstructure is observed leading to measured porosities below the maximum observed porosities at $T_f = 80°C$, as shown in figure 2*c*,*d*.

We proceed to explore two alternative hypotheses for cell wall failure which could lead to open-celled microstructures as observed for the PMMA nanofoams: (i) achievement of a critical hoop strain at the void at a critical value of porosity f_f or (ii) achievement of a minimum (critical) value of ligament thickness between neighbouring voids at a critical value of porosity f_c. A comparison of predictions with measured values of porosity is now given.

(a) Critical hoop strain

Assume that tearing of the cell wall occurs when the true (that is, logarithmic) value of hoop strain ε_s equals the T/T_g-dependent[20] true tensile failure strain ε_f. Recall that the solid surrounding the expanding void is incompressible. Then, by equation (4.1),

$$b^3 - a^3 = b_0^3 - a_0^3. \tag{5.1}$$

The initial (as-nucleated) porosity f_0 equals $(a_0/b_0)^3$ as defined in equation (4.23) and the current porosity f equals $(a/b)^3$. Now, rearrange equation (5.1), to express f as a function of f_0 and the true hoop strain ε_s at the surface of the void, where $\varepsilon_s = \varepsilon_{\theta\theta}(r = a) = \ln(a/a_0)$

$$f^{-1} = 1 + \exp(-3\varepsilon_s)(f_0^{-1} - 1). \tag{5.2}$$

Rupture of the cell wall occurs when $\varepsilon_s = \varepsilon_f$. The critical porosity f_f corresponding to this ductility-governed failure criterion reads

$$f_f^{-1} = 1 + \exp(-3\varepsilon_f)(f_0^{-1} - 1). \tag{5.3}$$

(b) Critical ligament size

The alternative failure hypothesis assumes that there is a minimum number of confined polymer chains separating individual cells to prevent rupture of the solid between the cells. Write h_c as the critical cell wall thickness, and assume that it is independent of T/T_g. Assume that the cell wall

[20]We assume ε_f to be insensitive to strain rate [24,53].

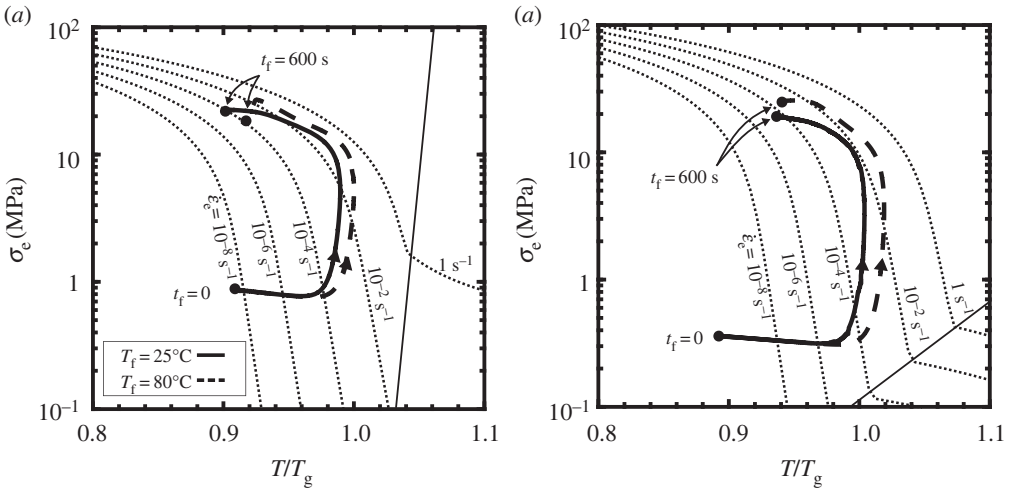

Figure 7. Deformation mechanism maps for (*a*) low M_w PMMA and (*b*) high M_w PMMA (for a reference strain $\varepsilon_{ref} = 0.05$), for contours of effective strain rate $\dot{\varepsilon}_e$. The predicted effective stress at the surface of the cavity σ_e is plotted as a function of T/T_g for foaming temperatures $T_f = 25$°C and $T_f = 80$°C and for a foaming time up to 600 s.

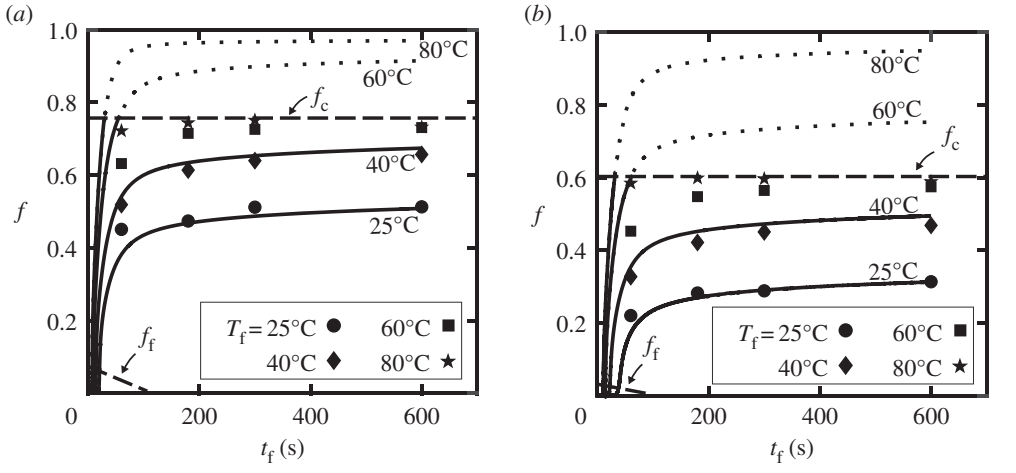

Figure 8. Predicted and measured porosity f versus foaming time t_f, for $T_f = 25$°C to $T_f = 80$°C for (*a*) the low M_w PMMA nanofoams and (*b*) the high M_w PMMA nanofoams. The ductility-governed porosity limit f_f is plotted via equation (5.3) for an initial porosity $f_0 = 10^{-3}$. The minimum cell wall thickness-governed porosity limit f_c is plotted via equation (5.5) for $f_0 = 10^{-3}$ and $h_c/a_0 = 3$ (low M_w PMMA) and $h_c/a_0 = 4.2$ (high M_w PMMA).

fails when the cell wall thickness reduces to this critical value, h_c. Define the smallest distance between two neighbouring cells h as

$$h = 2(b - a). \tag{5.4}$$

Then, upon making use of the expressions $f_0 = (a_0/b_0)^3$, $f = (a/b)^3$ and equation (5.2), we obtain

$$\frac{h}{a_0} = 2(f^{-1/3} - 1)\left(\frac{f_0^{-1} - 1}{f^{-1} - 1}\right)^{1/3}. \tag{5.5}$$

The corresponding critical value of porosity f_c is given by equation (5.5) with $h = h_c$.

The ductility-governed porosity limit f_f as given by equation (5.3) is plotted in figure 7 based on the predicted hoop strain ε_s during void growth. Note that we make use of the measured response of ε_f versus T/T_g (equation (B 2) for the low M_w PMMA and equation (B 1) for the high M_w PMMA as detailed in appendix B) and assume that the initial porosity $f_0 = 10^{-3}$. The measured values of final porosity f and the predictions of the void growth model exceed the porosity limit as given by f_f.

We now plot the porosity limit f_c in figure 7 via equation (5.5) for $f_0 = 10^{-3}$ by taking $h_c/a_0 = 3$ (low M_w PMMA) and $h_c/a_0 = 4.2$ (high M_w PMMA) in order to match to observed values of the maximum observed porosity f_{max} of the nanofoams. Recall that the initial void size a_0 of the low M_w PMMA nanofoams is estimated to be close to 10.5 nm, whereas a_0 is close to 5 nm for the high M_w PMMA nanofoams. Consequently, the estimated corresponding critical cell wall dimension $h_c = 32$ nm for the low M_w PMMA nanofoams, whereas $h_c = 21$ nm for the high M_w PMMA. These values for h_c are of the same order of magnitude as root-mean-square end-to-end distance R_{ee} of the PMMA chains, i.e. $R_{ee} \approx 20$ nm for the low M_w PMMA and $R_{ee} \approx 110$ nm for the high M_w PMMA based on an idealized equivalent freely jointed chain calculation [54]. This is in agreement with the results of Crosby and co-workers who conducted a series of uniaxial tensile tests on thin polystyrene (PS) films with $M_w = 136\,000$ g mol^{-1} [55,56]. They found that the tensile failure strain ε_f decreases with decreasing film thickness t in the regime $t = 15$–77 nm; these values are close to the estimated value for $R_{ee} = 25$ nm of the PS chains.

6. Concluding remarks

Solid-state nanofoaming experiments are performed on two grades of PMMA of markedly different molecular weight ($M_w = 92\,500$ g mol^{-1} and $M_w = 3\,580\,000$ g mol^{-1}). It was found that the molecular weight of the PMMA has a profound effect upon the microstructure of the PMMA nanofoams. When subjected to identical foaming conditions, the observed cell size $l \approx 35$ nm of the high molecular weight PMMA nanofoams is an order of magnitude less than that of the low molecular weight PMMA nanofoams, $l \approx 250$ nm. This is consistent with the observation that the nucleation density, $N_d \approx 20 \times 10^{20}$ m^{-3} of the high molecular weight PMMA nanofoams is an order of magnitude higher than that of the low molecular weight PMMA nanofoams $N_d \approx 2 \times 10^{20}$ m^{-3}. In addition, a limit in attainable porosity f_{max} was observed: $f_{max} = 0.65$ for the high molecular weight PMMA and $f_{max} = 0.75$ for the low molecular weight PMMA. The microstructure of the PMMA nanofoams transitions from closed-celled to open-celled at a porosity close to f_{max}.

A void growth model has been developed to simulate cavity expansion during solid-state nanofoaming of PMMA by CO_2. Experimentally calibrated constitutive laws for the PMMA grades close to the glass transition are used in the simulations. The predicted porosity of the nanofoams versus foaming time, at selected foaming temperatures, are in good agreement with the measured responses for porosities well below the maximum observed porosity. There is also close agreement between the predicted and observed sensitivity to molecular weight. This suggests that the observed difference in constitutive response close to the glass transition between the two PMMA grades leads to the measured difference in porosity. Moreover, cell wall tearing accounts for the observed limit in final porosity. Our analysis suggests the existence of a limiting minimum cell wall thickness of magnitude close to that of the end-to-end distance of the polymer chains. When the cell wall thickness approaches this minimum value during foaming, rupture of the cell walls occurs; this leads to an open-celled structure, and to a limit on foam expansion.

Data accessibility. Measurement data and code are available at the Cambridge University Apollo repository via https://doi.org/10.17863/CAM.43166.

Authors' contributions. V.B. and M.A.R.P. designed the foaming experiments. F.V.L. and V.B. conducted the foaming tests. F.V.L. and N.A.F. developed the void growth model. F.V.L. conducted the uniaxial tensile tests and drafted the manuscript. All other authors critically revised the manuscript. All authors gave final approval for publication.

Competing interests. We declare we have no competing interests.

Funding. Financial support from the Engineering and Physical Sciences Research Council (UK) award 1611305 (F.V.L.) and the FPU grant FPU14/02050 (V.B.) from the Spanish Ministry of Education is gratefully acknowledged. N.A.F. is grateful for additional financial support from the ERC project MULTILAT. Financial assistance from SABIC and MINECO/FEDER/UE (MAT2015-69234-R) is also acknowledged.
Acknowledgements. The authors thank Dr Martin van Es from SABIC for the technical assistance.

Appendix A. The assumption of uniform concentration of dissolved CO_2 within the spherical shell

At the start of the foaming process, the chemical potential of the CO_2 molecules in the nucleated voids is lower than the chemical potential of CO_2 molecules in the PMMA–CO_2 solid. Consequently, CO_2 gas molecules migrate from the PMMA–CO_2 solid into the voids. The concentration of CO_2 gas molecules $C(r, t)$ within the solid at time t and position r (for $a < r < b$) can be obtained by solving Fick's second law of diffusion [57]

$$\frac{\partial C}{\partial t} = \frac{D}{r^2}\frac{\partial}{\partial r}\left[r^2\frac{\partial C}{\partial r}\right], \tag{A 1}$$

in the deformed configuration, where D is the diffusion coefficient for CO_2 in PMMA. Measurements of D at temperatures and pressures typical for solid-state nanofoaming of PMMA by CO_2 are available in the literature as follows. Guo & Kumar [46] measured D based on desorption measurements and found that D ranges from $D = 2.5 \times 10^{-12}\,\mathrm{m^2\,s^{-1}}$ to $D = 3.65 \times 10^{-11}\,\mathrm{m^2\,s^{-1}}$ for temperatures ranging from −30°C to 100°C at a CO_2 pressure equal to 5 MPa. Li *et al.* [58] measured D by a sorption technique and found that D lies in the range of $6 \times 10^{-11}\,\mathrm{m^2\,s^{-1}}$ to $9.5 \times 10^{-11}\,\mathrm{m^2\,s^{-1}}$ for temperatures between 30°C and 70°C, and pressures between 6 MPa and 18 MPa. Now, introduce a characteristic diffusion time τ_D

$$\tau_D = \frac{(L_D)^2}{D}, \tag{A 2}$$

where L_D is a diffusion length which is approximated for the void growth problem by

$$L_D \approx b_0 \approx \left(\frac{3}{4\pi N_d}\right)^{1/3}. \tag{A 3}$$

Observations of cell nucleation densities of PMMA nanofoams ($N_d > 10^{20}\,\mathrm{m^{-3}}$) suggest that $L_D < 133$ nm [1]. Upon assuming $D = 10^{-12}\,\mathrm{m^2\,s^{-1}}$, we obtain $\tau_D \approx 20$ ms via equation (A 2), which is two orders of magnitude lower than typical observed foaming times for solid-state nanofoaming of PMMA by CO_2 as reported by Martín-de León *et al.* [9]. We conclude that the CO_2 concentration profile $C(R, t)$ is spatially uniform at all times: $C(R, t) = C(t)$. Consequently, we do not need to solve the diffusion equation to predict void growth during solid-state nanofoaming of PMMA by CO_2.

Appendix B. Calibration of the constitutive laws for PMMA

Constitutive laws are calibrated for the low M_w PMMA grade[21] close to its glass transition temperature. We follow the procedure of Van Loock & Fleck [24], who constructed deformation and failure maps for the high M_w PMMA grade[22] in uniaxial tension close to the glass transition temperature. A series of uniaxial tensile tests were performed on the low M_w PMMA grade for a range of temperatures ($T = 90$°C–170°C) and at a nominal strain rate $\dot{e} = 5.9 \times 10^{-2}\,\mathrm{s^{-1}}$. The dogbone specimen geometry and the measurement procedures are detailed in Van Loock & Fleck [24]. Note that the low M_w PMMA dogbone specimens are machined from the foaming precursor sheets. The true stress versus true strain responses of the low M_w PMMA dogbone

[21] Altuglas V825T with $T_g = 114.5$°C and $M_w = 92\,500\,\mathrm{g\,mol^{-1}}$.

[22] Altuglas CN with $T_g = 116.5$°C and $M_w = 3\,580\,000\,\mathrm{g\,mol^{-1}}$.

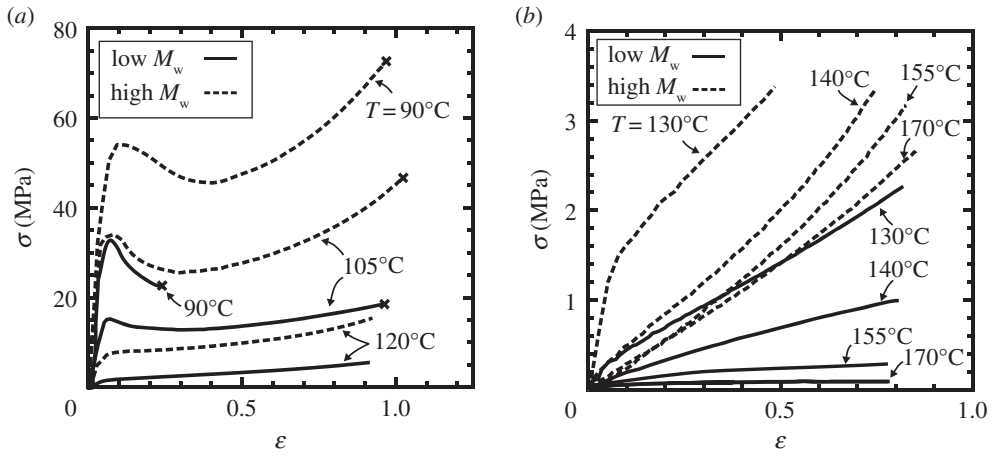

Figure 9. Measured true tensile stress σ versus true tensile strain ε curves for the low M_w and high M_w PMMA grades in uniaxial tension for a nominal strain rate $\dot{\varepsilon} = 5.9 \times 10^{-2}\,s^{-1}$ and for temperatures ranging from (*a*) $T = 90°C$ to $T = 120°C$ and (*b*) $T = 130°C$ to $T = 170°C$. A cross at the end of the curve denotes specimen failure.

specimens are plotted in figure 9*a* for $0.94 < T/T_g < 1.01$ and in figure 9*b* for $1.04 < T/T_g < 1.14$. The true stress versus true strain curves of the high M_w PMMA grade are included in figure 9*a*,*b*.

Loading–unloading uniaxial stress versus strain curves for the low M_w PMMA and high M_w PMMA are shown in figure 10. At $T/T_g = 0.93$, the elastic unloading of the low M_w and the high M_w PMMA occurs in the manner of an elasto-viscoplastic solid, with a remnant finite strain at zero load. The qualitative stress versus strain response of the low M_w and the high M_w PMMA is different when the temperature is increased to $T/T_g = 1.06$. The elastic rubbery regime is entered for the high M_w PMMA and the unloading curve is almost coincidental with the loading curve; there is negligible hysteresis and negligible remnant strain. No rubbery regime is observed for the low M_w PMMA above the glass transition. At $T/T_g = 1.06$ and $T/T_g = 1.12$, the stress versus strain response of the low M_w PMMA in uniaxial tension is linear viscous. Unloading is accompanied by a finite remnant strain. The high M_w PMMA transitions from the rubbery regime to a viscous regime at $T/T_g = 1.16$.

First, consider the elasto-viscoplastic regime. The dependence of the measured flow strength σ_y of the low M_w and high M_w PMMA grades upon T/T_g is shown in figure 11 for $\dot{e} = 5.9 \times 10^{-2}\,s^{-1}$. A single transition Ree–Eyring equation, equation (4.18), is fitted to the σ_y versus T/T_g response of the low M_w PMMA in the glassy and glass transition regime (corresponding to $0.94 \le T/T_g \le 1.04$). We assume that $q = 7.31 \times 10^{-19}\,J$ and $\dot{\varepsilon}_0 = 1.5 \times 10^{56}\,s^{-1}$ for both the low M_w and the high M_w PMMA, as reported by Van Loock & Fleck [24]. The activation volume $v = 2.5\,nm^{-3}$ for the low M_w PMMA, and $v = 1.8\,nm^{-3}$ for the high M_w PMMA [24]. The resulting curve fits are included in figure 11. Second, consider the viscous regime for the low M_w PMMA. We fit a linear, viscous constitutive law, equations (4.20) and (4.21), to the measured σ_y versus T/T_g curves of the low M_w PMMA in the regime of $1.06 \le T/T_g \le 1.14$ and $\dot{e} = 5.9 \times 10^{-2}\,s^{-1}$. The fitting values are $\eta_0 = 2.8 \times 10^6\,Pa\,s$, $C_1 = 3.2$ and $C_2 = 17.3\,K$. The resulting curve fit is adequate, see figure 11. Third, consider the rubbery regime of the high M_w PMMA. The constitutive description, equation (4.19), is adequate upon making use of previously measured values ($E_R^0 = 65.8\,MPa$, $\alpha_R = 0.80$, $\dot{\varepsilon}_R = 1.58\,s^{-1}$ and $n = 0.173$ [24]), as shown in figure 11.

(a) Tensile ductility of the low M_w and high M_w PMMA

Van Loock & Fleck [24] measured the true tensile failure strain, that is ductility, ε_f of the high M_w PMMA grade by testing a dogbone geometry at $T/T_g < 1$ and an hourglass-shaped specimen geometry at $T/T_g \ge 1$. The measured values for ε_f of the high M_w PMMA grade are plotted as

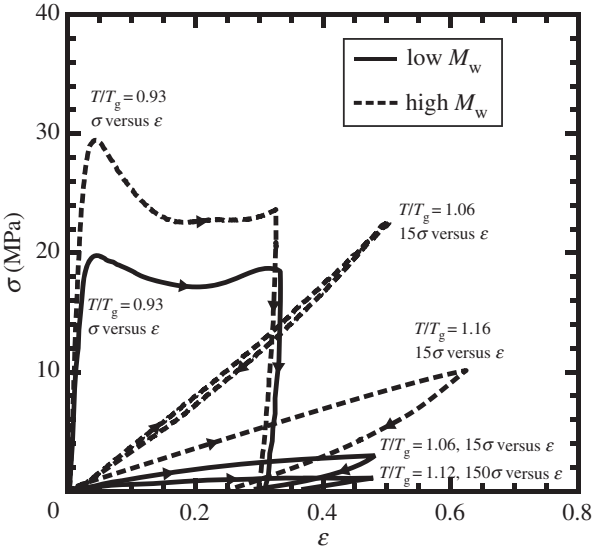

Figure 10. Loading–unloading true stress versus true strain curves for the low M_w PMMA and high M_w PMMA grades in uniaxial tension, at selected values of T/T_g, for a nominal strain rate $\dot{\varepsilon} = 5.9 \times 10^{-4}\text{s}^{-1}$.

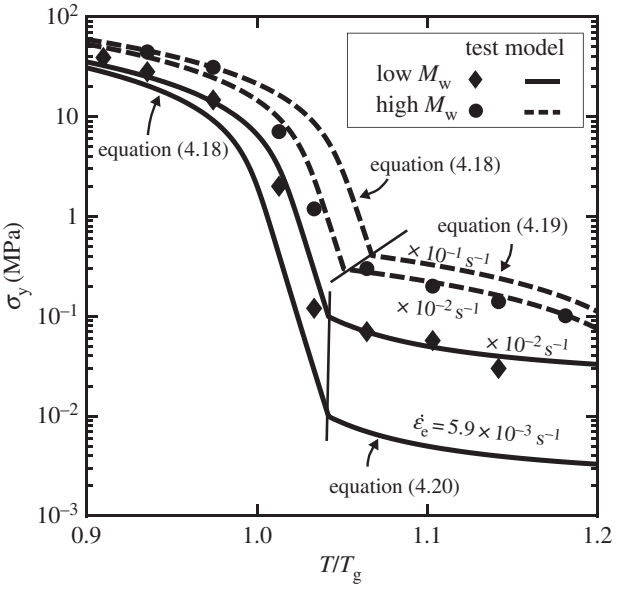

Figure 11. Deformation mechanism maps of the low M_w and high M_w PMMA grades. Flow strength σ_y $(=\sigma_e)$ versus T/T_g is plotted, with the curve fits of the constitutive models included for a reference strain $\varepsilon_{ref} = 0.05$.

a function of the normalized temperature T/T_g for a nominal strain rate $\dot{e} = 5.9 \times 10^{-2}\,\text{s}^{-1}$ in figure 12. The ε_f versus T/T_g failure envelope is adequately fitted by a linear relation [24]

$$\varepsilon_f = 7.3\frac{T}{T_g} - 6.3. \tag{B 1}$$

An additional series of uniaxial tensile tests has been conducted on the low M_w PMMA grade by using the same measurement methods as that detailed in the work of Van Loock &

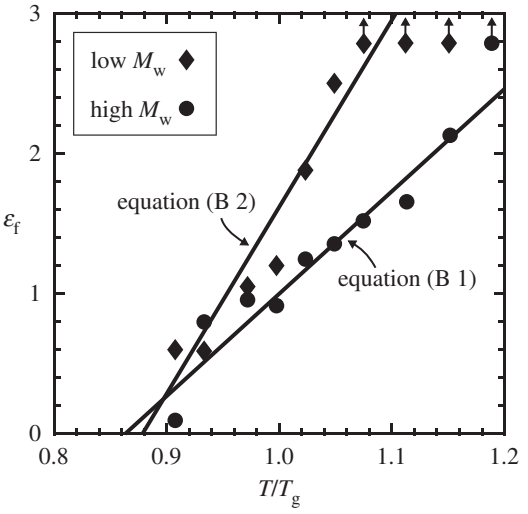

Figure 12. The measured true tensile failure strain ε_f as a function of normalized testing temperature T/T_g for the low M_w and high M_w PMMA grades, at a nominal strain rate $\dot{\varepsilon} = 5.9 \times 10^{-2}\ s^{-1}$.

Fleck [24]. No failure was observed at $T \geq 145°C$ prior to the attainment of the maximum cross-head extension. The measured ε_f versus T/T_g curve is shown in figure 12. The failure envelope of the low M_w PMMA grade close to the glass transition is also fitted by a linear relation

$$\varepsilon_f = 13.3\frac{T}{T_g} - 11.7. \tag{B 2}$$

References

1. Costeux S. 2014 CO_2-blown nanocellular foams. *J. Appl. Polym. Sci.* **131**, 41293. (doi:10.1002/app.41293)
2. Notario B, Pinto J, Rodríguez-Pérez MÁ. 2015 Towards a new generation of polymeric foams: PMMA nanocellular foams with enhanced physical properties. *Polymer* **63**, 116–126. (doi:10.1016/j.polymer.2015.03.003)
3. Miller D, Kumar V. 2009 Microcellular and nanocellular solid-state polyetherimide (PEI) foams using sub-critical carbon dioxide I. Processing and structure. *Polymer* **50**, 5576–5584. (doi:10.1016/j.polymer.2011.04.049)
4. Martín-de León J, Bernardo V, Rodríguez-Pérez MÁ. 2017 Key production parameters to obtain transparent nanocellular PMMA. *Macromol. Mater. Eng.* **302**, 3–7. (doi:10.1002/mame.201700343)
5. Schmidt D, Raman VI, Egger C, du Fresne C, Schadler V. 2007 Templated cross-linking reactions for designing nanoporous materials. *Mater. Sci. Eng. C* **27**, 1487–1490. (doi:10.1016/j.msec.2006.06.028)
6. Notario B, Pinto J, Solorzano E, de Saja JA, Dumon M, Rodríguez-Pérez MÁ. 2014 Experimental validation of the Knudsen effect in nanocellular polymeric foams. *Polymer* **56**, 57–67. (doi:10.1016/j.polymer.2014.10.006)
7. Wang G, Wang C, Zhao J, Wang G, Park CB, Zhao G. 2017 Modelling of thermal transport through a nanocellular polymer foam: toward the generation of a new superinsulating material. *Nanoscale* **9**, 5996–6009. (doi:10.1039/C7NR00327G)
8. Martini JE. 1981 The production and analysis of microcellular foam. PhD thesis. USA: MIT.
9. Martin-de León J, Bernardo V, Rodríguez-Pérez MÁ. 2016 Low density nanocellular polymers based on PMMA produced by gas dissolution foaming: fabrication and cellular structure characterization. *Polymers (Basel).* **8**, 256. (doi:10.3390/polym8070265)

10. Guo H, Nicolae A, Kumar V. 2015 Solid-state poly(methyl methacrylate) (PMMA) nanofoams. Part II: low-temperature solid-state process space using CO_2 and the resulting morphologies. *Polymer* **70**, 231–241. (doi:10.1016/j.polymer.2015.06.031)
11. Martín-de León J, Bernardo V, Rodríguez-Pérez MÁ. 2019 Nanocellular polymers: the challenge of creating cells in the nanoscale. *Materials (Basel).* **12**, 797. (doi:10.3390/ma12050797)
12. Bernardo V, Martin-de Leon J, Pinto J, Catelani T, Athanassiou A, Rodriguez-Perez MA. 2019 Low-density PMMA/MAM nanocellular polymers using low MAM contents: production and characterization. *Polymer* **163**, 115–124. (doi:10.1016/j.polymer.2018.12.057)
13. Bernardo V, Van Loock F, Martin-de Leon J, Fleck NA, Rodriguez-Perez MA. 2019 Mechanical properties of PMMA-sepiolite nanocellular materials with a bimodal cellular structure. *Macromol. Mater. Eng.* **304**, 1900041. (doi:10.1002/mame.201900041)
14. Wang G, Zhao J, Mark LH, Wang G, Yu K, Wang C, Park CB, Zhao G. 2017 Ultra-tough and super thermal-insulation nanocellular PMMA/TPU. *Chem. Eng. J.* **325**, 632–646. (doi:10.1016/j.cej.2017.05.116)
15. Costeux S, Zhu L. 2013 Low density thermoplastic nanofoams nucleated by nanoparticles. *Polymer* **54**, 2785–2795. (doi:10.1016/j.polymer.2013.03.052)
16. Costeux S, Khan I, Bunker SP, Jeon HK. 2014 Experimental study and modeling of nanofoams formation from single phase acrylic copolymers. *J. Cell. Plast.* **51**, 197–221. (doi:10.1177/0021955X14531972)
17. Reglero Ruiz JA, Dumon M, Pinto J, Rodriguez-Pérez MA. 2011 Low-density nanocellular foams produced by high-pressure carbon dioxide. *Macromol. Mater. Eng.* **296**, 752–759. (doi:10.1002/mame.201000346)
18. Wang G, Zhao G, Zhang L, Mu Y, Park CB. 2018 Lightweight and tough nanocellular PP/PTFE nanocomposite foams with defect-free surfaces obtained using in situ nanofibrillation and nanocellular injection molding. *Chem. Eng. J.* **350**, 1–11. (doi:10.1016/j.cej.2018.05.161)
19. Street JR. 1968 The rheology of phase growth in elastic liquids. *J. Rheol.* **12**, 103. (doi:10.1122/1.549101)
20. Amon M, Denson CD. 1984 A study of the dynamics of foam growth: analysis of the growth of closely spaced spherical bubbles. *Polym. Eng. Sci.* **24**, 1026–1034. (doi:10.1002/pen.760241306)
21. Venerus DC, Yala N, Bernstein B. 1998 Analysis of diffusion-induced bubble growth in viscoelastic liquids. *J. Nonnewton. Fluid Mech.* **75**, 55–75. (doi:10.1016/S0377-0257(97)00076-1)
22. Khan I, Adrian D, Costeux S. 2015 A model to predict the cell density and cell size distribution in nano-cellular foams. *Chem. Eng. Sci.* **138**, 634–645. (doi:10.1016/j.ces.2015.08.029)
23. Shafi MA, Lee JG, Flumerfelt RW. 1996 Prediction of cellular structure in free expansion polymer foam processing. *Polym. Eng. Sci.* **36**, 1950–1959. (doi:10.1002/pen.10591)
24. Van Loock F, Fleck NA. 2018 Deformation and failure maps for PMMA in uniaxial tension. *Polymer* **148**, 259–268. (doi:10.1016/j.polymer.2018.06.027)
25. Rides M, Morikawa J, Halldahl L, Hay B, Lobo H, Dawson A, Allen C. 2009 Intercomparison of thermal conductivity and thermal diffusivity methods for plastics. *Polym. Test.* **28**, 480–489. (doi:10.1016/j.polymertesting.2009.03.002)
26. Pinto J, Solórzano E, Rodriguez-Perez MA, De Saja JA. 2013 Characterization of the cellular structure based on user-interactive image analysis procedures. *J. Cell. Plast.* **49**, 555–575. (doi:10.1177/0021955X13503847)
27. Kumar V, Suh NP. 1990 A process for making microcellular thermoplastic parts. *Polym. Eng. Sci.* **30**, 1323–1329. (doi:10.1002/pen.760302010)
28. ASTM D6226-15 2015 *Standard test method for open cell content of rigid cellular plastics*. West Conshohocken, PA, USA: ASTM International.
29. Goel SK, Beckman EJ. 1995 Nucleation and growth in microcellular materials: supercritical CO_2 as foaming agent. *AIChe* **41**, 357–367. (doi:10.1002/aic.690410217)
30. Timoshenko SP, Goodier JN. 2001 *Theory of elasticity*. New York, NY: McGraw-Hill.
31. Hill R. 1950 *The mathematical theory of plasticity*. New York, NY: Oxford University Press.
32. Rajendran A, Bonavoglia B, Forrer N, Storti G, Mazzotti M, Morbidelli M. 2005 Simultaneous measurement of swelling and sorption in a supercritical CO_2-poly(methyl methacrylate) system. *Ind. Eng. Chem. Res.* **44**, 2549–2560. (doi:10.1021/ie049523w)
33. Pantoula M, Panayiotou C. 2006 Sorption and swelling in glassy polymer/carbon dioxide systems. *J. Supercrit. Fluids* **37**, 254–262. (doi:10.1016/j.supflu.2005.11.001)

34. Pantoula M, von Schnitzler J, Eggers R, Panayiotou C. 2007 Sorption and swelling in glassy polymer/carbon dioxide systems. Part II-Swelling. *J. Supercrit. Fluids* **39**, 426–434. (doi:10.1016/j.supflu.2006.03.010)
35. Van Krevelen DW, Te Nijenhuis K. 2009 *Properties of polymers*. Amsterdam, the Netherlands: Elsevier.
36. Sanchez IC, Lacombe RH. 1974 Theory of liquid-liquid and liquid-vapour equilibria. *Nature* **251**, 281–283. (doi:10.1038/252497a0)
37. Sanchez IC, Lacombe RH. 1976 An elementary molecular theory of classical fluids. Pure fluids. *J. Phys. Chem.* **80**, 2352–2362. (doi:10.1021/j100562a008)
38. Sanchez IC, Lacombe RH. 1978 Statistical thermodynamics of polymer solutions. *Macromolecules* **11**, 1145–1156. (doi:10.1021/ma60066a017)
39. Von Konigslow K, Park CB, Thompson RB. 2017 Polymeric foaming predictions from the Sanchez-Lacombe equation of state: application to polypropylene-carbon dioxide mixtures. *Phys. Rev. Appl.* **8**, 1–14. (doi:10.1103/PhysRevApplied.8.044009)
40. Span R, Wagner W. 1996 A new equation of state for carbon dioxide covering the fluid region from the triple-point temperature to 1100 K at pressures up to 800 MPa. *J. Phys. Chem. Ref. Data* **25**, 1509–1596. (doi:10.1063/1.555991)
41. Huang FH, Li MH, Lee LL, Starling KE, Chung FTH. 1985 Accurate equation of state for carbon dioxide. *J. Chem. Eng. Japan* **18**, 490–496. (doi:10.1252/jcej.18.490)
42. Alessi P, Cortesi A, Kikic I, Vecchione F. 2003 Plasticization of polymers with supercritical carbon dioxide: experimental determination of glass-transition temperatures. *J. Appl. Polym. Sci.* **88**, 2189–2193. (doi:10.1002/app.11881)
43. Verreck G, Decorte A, Li H, Tomasko D, Arien A, Peeters J, Rombaut P, Van den Mooter G, Brewster ME. 2006 The effect of pressurized carbon dioxide as a plasticizer and foaming agent on the hot melt extrusion process and extrudate properties of pharmaceutical polymers. *J. Supercrit. Fluids* **38**, 383–391. (doi:10.1016/j.supflu.2005.11.022)
44. Chiou JS, Barlow JW, Paul DR. 1985 Plasticization of glassy polymers by CO_2. *J. Appl. Polym. Sci.* **30**, 2633–2642. (doi:10.1002/app.1985.070300626)
45. Wissinger RG, Paulaitis ME. 1991 Glass transitions in polymer/CO_2 mixtures at elevated pressures. *J. Polym. Sci. Part B Polym. Phys.* **29**, 631–633. (doi:10.1002/polb.1991.090290513)
46. Guo H, Kumar V. 2015 Solid-state poly(methyl methacrylate) (PMMA) nanofoams. Part I: low-temperature CO_2 sorption, diffusion, and the depression in PMMA glass transition. *Polymer* **57**, 157–163. (doi:10.1016/j.polymer.2014.12.029)
47. Chow S. 1980 Molecular interpretation of the glass transition temperature of polymer-diluent systems. *Macromolecules* **364**, 362–364. (doi:10.1021/ma60074a029)
48. Li R, Li L, Zeng D, Liu Q, Fang T. 2016 Numerical selection of the parameters in producing microcellular polymethyl methacrylate with supercritical CO_2. *Cell. Polym.* **35**, 309–328. (doi:10.1177/026248931603500602)
49. McLoughlin JR, Tobolsky AV. 1952 The viscoelastic behavior of polymethyl methacrylate. *J. Colloid Sci.* **7**, 555–568. (doi:10.1016/0095-8522(52)90039-1)
50. Williams ML, Landel RF, Ferry JD. 1955 The temperature dependence of relaxation mechanisms in amorphous polymers and other glass-forming liquids. *J. Am. Chem. Soc.* **77**, 3701–3707. (doi:10.1021/ja01619a008)
51. Bin Ahmad Z, Ashby MF. 1988 Failure-mechanism maps for engineering polymers. *J. Mater. Sci.* **23**, 2037–2050. (doi:10.1007/BF01115766)
52. Carslaw HS, Jaeger JC. 1959 *Conduction of heat in solids*, 2nd edn. Oxford, UK: Clarendon Press.
53. Cheng WM, Miller GA, Manson JA, Hertzberg RW, Sperling LH. 1990 Mechanical behaviour of poly(methyl methacrylate). *J. Mater. Sci.* **25**, 1931–1938. (doi:10.1007/BF01045745)
54. Rubinstein M, Colby HR. 2003 *Polymer physics*. Oxford, UK: Oxford University Press.
55. Liu Y, Chen YC, Hutchens S, Lawrence J, Emrick T, Crosby AJ. 2015 Directly measuring the complete stress-strain response of ultrathin polymer films. *Macromolecules* **48**, 6534–6540. (doi:10.1021/acs.macromol.5b01473)
56. Bay RK, Shimomura S, Liu Y, Ilton M, Crosby AJ. 2018 Confinement effect on strain localizations in glassy polymer films. *Macromolecules* **51**, 3647–3653. (doi:10.1021/acs.macromol.8b00385)
57. Crank J. 1979 *The mathematics of diffusion*. Oxford, UK: Clarendon Press.
58. Li R, Ye N, Shaayegan V, Fang T. 2018 Experimental measurement of CO_2 diffusion in PMMA and its effect on microcellular foaming. *J. Supercrit. Fluids* **135**, 180–187. (doi:10.1016/j.supflu.2018.01.024)